may result from long-term fluctuations of the general circulation of the stratosphere, such as a decrease in the strength of the Brewer-Dobson circulation. However, measurements of the stratospheric circulation are sparse, and inferring the transport of photochemically active trace species is difficult. The Upper Atmosphere Research Satellite (scheduled to be launched in the early 1990s) should improve our understanding of the stratospheric circulation and allow a better evaluation of the relative importance of the various loss mechanisms.

REFERENCES AND NOTES

1. J. C. Farman, B. G. Gardiner, J. D. Shanklin, *Nature (London)* **315**, 207 (1985).
2. R. S. Stolarski *et al.*, *ibid.* **322**, 808 (1986).
3. K. P. Bowman, *Geophys. Res. Lett.* **13**, 1193 (1986).
4. G. M. B. Dobson, *Q. J. R. Meteorol. Soc.* **92**, 549 (1966).
5. Most of the available data on the ozone hole, including observations of ozone, other trace species, and the atmospheric circulation, were presented in a special issue of *Geophysical Research Letters* [vol. 13, no. 12 (1986)].
6. National Research Council, *Halocarbons: Effects on Stratospheric Ozone* (National Academy of Sciences, Washington, DC, 1976); *Stratospheric Ozone Depletion by Halocarbons: Chemistry and Transport* (National Academy of Sciences, Washington, DC, 1979); *Causes and Effects of Stratospheric Ozone Reduction: An Update* (National Academy of Sciences, Washington, DC, 1982); "Atmospheric Ozone," *World Meteorol. Organ. Rep. No. 16* (World Meteorological Organization, Geneva, 1985).
7. S. Solomon, R. R. Garcia, F. S. Rowland, D. J. Wuebbles, *Nature (London)* **321**, 755 (1986); M. B. McElroy, R. J. Salawitch, S. C. Wofsy, J. A. Logan, *ibid.*, p. 759.
8. K.-K. Tung, M. K. W. Ko, J. M. Rodriguez, N. D. Sze, *ibid.* **322**, 811 (1986); J. D. Mahlman and S. B. Fels, *Geophys. Res. Lett.* **13**, 1316 (1986).
9. TOMS ozone data are processed by the Ozone Processing Team at NASA Goddard Space Flight Center (GSFC) under the direction of D. Heath. Data are available from the National Space Science Data Center at GSFC.
10. K. P. Bowman and A. J. Krueger, *J. Geophys. Res.* **90**, 7967 (1985).
11. A. J. Fleig *et al.*, *Geophys. Res. Lett.* **13**, 1355 (1986); A. J. Fleig, P. K. Bhartia, D. S. Silberstein, *ibid.*, p. 1359.
12. A. M. Bass and R. J. Paur, in *Atmospheric Ozone, Proceedings of the Quadrennial Ozone Symposium, 1984*, C. S. Zerefos and A. Ghazi, Eds. (Reidel, Dordrecht, 1985), p. 611.
13. P. K. Bhartia, K. F. Klenk, C. K. Wong, D. Gordon, *J. Geophys. Res.* **89**, 5239 (1984).
14. J. London and S. J. Oltmans, *Pure Appl. Geophys.* **117**, 345 (1978).
15. R. R. Garcia and S. Solomon, *Geophys. Res. Lett.* **14**, 848 (1987).
16. J. K. Angell, *Mon. Weather Rev.* **115**, 753 (1987).
17. R. B. Rood, *Geophys. Res. Lett.* **13**, 1244 (1986).

18. This work was supported by the NASA Upper Atmosphere Theory and Data Analysis Program through grant NAGW-992 to the University of Illinois at Urbana-Champaign.

21 August 1987; accepted 17 November 1987

Atomic Force Microscopy of an Organic Monolayer

O. MARTI, H. O. RIBI, B. DRAKE, T. R. ALBRECHT, C. F. QUATE, P. K. HANSMA

Atomic force microscope images of polymerized monolayers of *n*-(2-aminoethyl)-10,12-tricosadiynamide revealed parallel rows of molecules with a side-by-side spacing of ≈0.5 nanometer. Forces used for imaging (10^{-8} newton) had no observable effect on the polymer strands. These results demonstrate that atomic force microscope images can be obtained for an organic system.

THE ATOMIC FORCE MICROSCOPE (AFM) (*1–5*) is a new instrument suitable for imaging surfaces. The images consist of a series of parallel profiles of a surface. Each profile is obtained by moving a tip, which ideally is terminated by a single atom, across the surface with a small tracking force on the order of 10^{-8} N. Predecessors of this instrument include profilometers (*6–8*), the topografiner (*9*), and scanning tunneling microscopes (STM) (*10, 11*). The AFM, unlike the STM, is not restricted to conductive or semiconductive surfaces. Atomic resolution imaging (*2, 4*) that approaches the resolving power of STMs and is much better than that of stylus profilometers has been demonstrated with AFMs. We report AFM images of organic molecules.

Our AFM design is an extension of an earlier STM design (*12*) and an improved version of the first operational AFM design (*4*) by our group. As shown in Fig. 1, the sample is mounted on an (x,y,z) scanner (*13*) and pressed against a diamond tip mounted on a triangular microcantilever (*5*) with a spring constant of ≈1 N/m. The deflection of the microcantilever is monitored by sensing the tunneling current between the back of the microcantilever and a platinum-iridium point. Deflections for the data reported were on the order of 10 nm, which resulted in forces between the tip and the sample on the order of 10^{-8} N. During imaging the deflection was kept constant by a feedback loop that controlled the height z of the sample.

The dominant mass of the microcantilever–diamond tip assembly in our microscope is the mass of the diamond tip (≈1×10^{-10} kg). This mass and the spring constant of the cantilever together give a resonant frequency of ≈16 kHz, which is in agreement with the performance of the microscope. The repulsive interaction with the surface creates another spring in parallel to the cantilever and increases the overall resonant frequency during operation.

We imaged polymerized monolayers of AE-TDA [*n*-(2-aminoethyl)-10,12-tricosadiynamide] because this compound is well defined chemically and films in the polymerized state show a high degree of structural integrity when transferred to glass supports. This compound was prepared as the polymerizable surfactant by attaching ethylenediamine through the amide linkage to 10,12-tricosadiynoic acid.

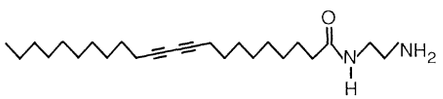

1

Monolayers of AE-TDA were formed at the air-water interface by standard methods (*14*). The films were compressed to near their collapse pressure (~0.05 N/m) to ensure that they were in a crystalline state, and they were then polymerized by ultraviolet irradiation. The films had a pink-blue appearance indicative of the conjugated polydiacetylene polymer (*15*). After polymerization, the monolayers were transferred to glass chips with the hydrophilic side of the film abutting to the surface of the glass. Attachment of the monolayers to the glass surface was confirmed by fluorescent microscopy. The polymer layers appeared bright orange-red under magnifications of ×40 to ×200 when the light was filtered with a rhodamine filter. The monolayers were comprised of tightly packed microcrystalline domains between 1 and 100 μm in diameter and covered a total surface area of 70 to 80%. Domains similar in dimension and distribution were observed by transmission electron microscopy when the polymerized monolayers were transferred to nitrocellulose-coated microscope grids (*16*).

O. Marti, B. Drake, P. K. Hansma, Department of Physics, University of California, Santa Barbara, CA 93106.
H. O. Ribi, Department of Cell Biology, Stanford University, Stanford, CA 94305.
T. R. Albrecht and C. F. Quate, Edward L. Ginzton Laboratory, W. W. Hansen Laboratories of Physics, Stanford University, Stanford, CA 94305.

Figure 2, A and B, are recordings of the z voltage on the (x,y,z) scanner, which was controlled by a feedback loop to keep the deflection of the microcantilever and hence the force applied to the sample constant. In the absence of polymerized monolayers, AFM images of clean glass surfaces appeared free of corrugation (Fig. 2A). Images of AE-TDA deposited on glass revealed parallel rows with a side-by-side spacing of roughly 0.55 ± 0.05 nm and a corrugation of 0.1 ± 0.05 nm (Fig. 2B). The size of the displayed area and the height scale in the contrast are the same in A and B of Fig. 2. We kept the z voltage on the (x,y,z) scanner constant and recorded the fluctuations in the tunneling current between the platinum-iridium point and the microcantilever tracking the sample surface. We observed the same rowlike structures on another region of the AE-TDA sample after we moved it mechanically. However, the rows were at a different angle, as the sample had domains with different alignments. We moved the imaging window electrically over the surface and always observed the same rowlike structures with the same orientation. The total accessible area of 0.3 μm by 0.3 μm (without mechanical movement of the sample) made the observation of two domains with different orientations and a diameter of 1 to 100 μm unlikely. The observed features appeared to be real and not artifacts because (i) domains were observed with varying orientation in different runs; (ii) images of base substrates (clean glass) showed no structure; (iii) the side-by-side distance between the rows was unaffected by the scanning speed; (iv) the number of rows was proportional to the window size; and (v) the AE-TDA structure could be detected in a number of locations.

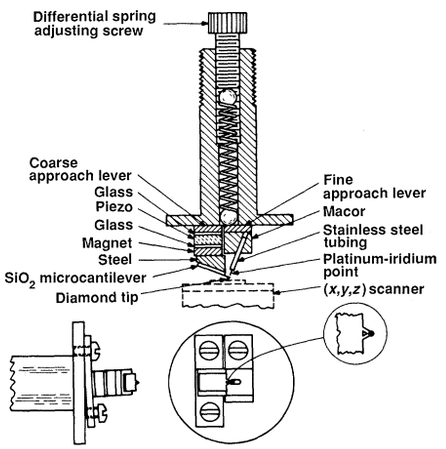

Fig. 1. Setup of the AFM. The sample, a glass substrate with the AE-TDA monolayer, is shown by dashed lines. It is attached to the center of the (x,y,z) scanner by a phosphorous bronze clamp and pressed against the tip of the force sensor. The central mounting minimizes the interferences and distortions that a signal on one axis in an (x,y,z) scanner of the single-tube design imposes on the other axes. The silicon chip holding the silicon dioxide microcantilever is glued to a steel wedge that has a 20° angle. The steel wedge is held in place by a magnet on the force sensor, allowing easy positioning opposite to the platinum-iridium point and fast replacement of the microcantilever. The approach of the point to the cantilever is achieved in three steps. The coarse approach lever with the cantilever (inset lower left) is used to lower the gap between point and cantilever to ≈10 μm. Further reduction is achieved with the differential spring mechanism that consists of the differential spring adjusting screw and its associated spring and ball and the fine approach lever holding the tip. The last stage of adjustment is the piezo located between the magnet and the coarse approach lever. To achieve a well-defined sharp tip, we used either a piece of diamond dust (*19*) 40 to 60 μm wide or a fragment of a shattered diamond (*4*) (inset lower right). During the experiment the microscope was in a plexiglass can to isolate it from sound and moving air. This can was on a concrete block suspended from the ceilings by rubber bungee cords. All the cables running to the concrete block were attached to heavy weights on the block for vibration isolation. The (x,y,z) scanner of the microscope was calibrated by imaging highly oriented pyrolytic graphite while in an STM mode (*4*).

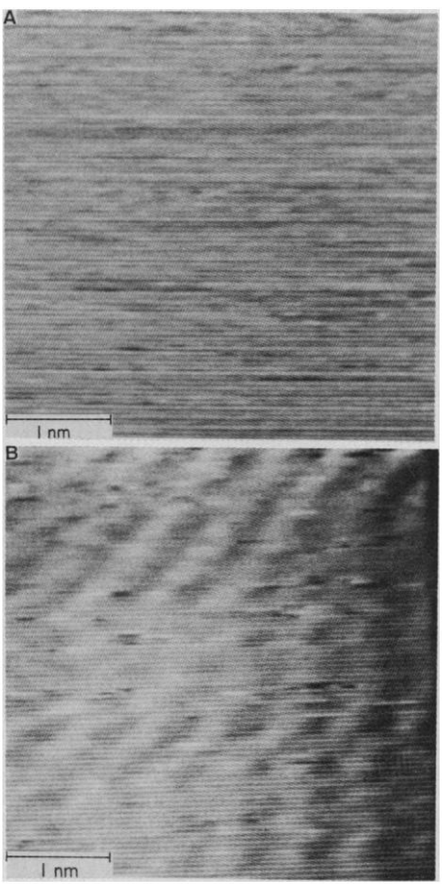

Fig. 2. AFM images of the surface of a glass slide (**A**) and of AE-TDA deposited on the surface of glass (**B**). There are rows of molecules with a side-by-side spacing of ≈0.5 nm. White corresponds to protrusions on the sample and black to depressions in these gray-scale images. Both images have identical scanning windows and gray scales and consist of 250 lines with 256 pixels. The images, corrected by subtraction of the background plane, were captured with an Arlunya temporal filter and image storage device (*20*).

The repeat distance between the rows was in agreement with the lattice dimensions and polymer packing in monolayers of a related diacetylenic compound (*17*). The image of the hydrophobic side of the AE-TDA monolayer consists of the images of the top ends of the single molecules polymerized into the monolayer. Polymerization occurs along one direction, which varies for different domains. The observation of rows in Fig. 2B rather than of single AE-TDA ends is presumably a result of the tighter binding of the hydrocarbon tails along the polymerization direction, which restricts the possible direction of relaxation under the load of the AFM tip. Although some structure is visible along the rows, we cannot make any quantitative statements at this time.

Resolution of unstained or negatively stained monolayers of AE-TDA by means of transmission electron microscopy was not sufficient for resolving the molecular details observed by AFM (*16*). Our AFM is not yet, however, useful for routine imaging of biological materials. Further improvements in the diamond tip preparation and cleaning, protection against accidental breakage of the microcantilevers, and the development of calibration samples are necessary. Recently, an AFM was operated on samples under paraffin oil (*4*), a nonpolar fluid. The STMs may be operated under water and aqueous solutions (*12, 18*), and there is no fundamental difficulty in adding the spring and tip for an AFM.

REFERENCES AND NOTES

1. G. Binnig, C. F. Quate, Ch. Gerber, *Phys. Rev. Lett.* **12**, 930 (1986).
2. G. Binnig, Ch. Gerber, E. Stoll, T. R. Albrecht, C. F. Quate, *Europhys. Lett.* **3**, 1281 (1987).
3. G. M. McClelland, R. Erlandsson, S. Chiang, in *Review of Progress in Quantitative Nondestructive Evaluation*, D. O. Thompson and D. E. Chimenti, Eds. (Plenum, New York, 1987), vol. 6B, p. 1307.
4. O. Marti, B. Drake, P. K. Hansma, *Appl. Phys. Lett.* **51**, 484 (1987).
5. T. R. Albrecht and C. F. Quate, *J. Appl. Phys.* **62**, 2599 (1987).
6. J. B. P. Williamson, *Proc. Inst. Mech. Eng.* **182**, 21 (1967).
7. K. H. Günther, P. G. Wierer, J. M. Bennet, *Appl. Opt.* **23**, 3820 (1984).
8. E. C. Teague, F. E. Scire, S. M. Backer, S. W. Jensen, *Wear* **83**, 1 (1982).
9. R. Young, J. Ward, F. Scire, *Rev. Sci. Instrum.* **43**, 999 (1972).
10. G. Binnig and H. Rohrer, *Helv. Phys. Acta* **55**, 726 (1982).
11. Two recent reviews are by C. F. Quate [*Phys. Today* **39**, 26 (August 1986)] and P. K. Hansma and J. Tersoff [*J. Appl. Phys.* **61**, R1 (1987)].
12. R. Sonnenfeld, J. Schneir, B. Drake, P. K. Hansma, D. E. Aspens, *Appl. Phys. Lett.* **50**, 1742 (1987).
13. G. Binnig and D. P. E. Smith, *Rev. Sci. Instrum.* **57**, 1688 (1986).

14. G. L. Gaines, Jr., *Insoluble Monolayers at Liquid-Gas Interfaces*, I. Prigogine, Ed. (Wiley, New York, 1966).
15. D. R. Day and H. Ringsdorf, *Makromol. Chem.* **180**, 1059 (1979).
16. H. O. Ribi, unpublished results.
17. D. Day and J. B. Lando, *Macromolecules* **13**, 1478 (1980); *ibid.*, p. 1483.
18. R. Sonnenfeld and P. K. Hansma, *Science* **232**, 211 (1986).
19. Diamond dust: 40 to 60 μm wide, Aesar 070286; glue: tiny amounts of Epoxi-Patch from Hysol Division, the Dexter Corporation.
20. Arlunya TF5000 Image Processor, Princeton Electronic Products.
21. We thank the staff of the University of California, Santa Barbara (UCSB), Physics Machine Shop and especially M. Wilson, R. Stuber, and K. Voelker for helping to build the microscope; G. N. Patel for his gift of 10,12-tricosadiynoic acid; the UCSB Physics Electronic Shop staff; E. Martzen and A. Dietler for secretarial assistance; R. Kornberg, G. Binnig, D. Smith, J. Schneir, R. Sonnenfeld, and S. Alexander for useful discussions. This work was supported in part by the Office of Naval Research, by the Joint Services Electronics Program at Stanford University, and by a grant from the Swiss National Science Foundation (O.M.). H.O.R. received support from Cellular and Molecular Biology Training grant GM07276-12 from NIH.

15 July 1987; accepted 16 October 1987

GEOSAT Altimeter Observations of Kelvin Waves and the 1986–87 El Niño

LAURY MILLER, ROBERT E. CHENEY, BRUCE C. DOUGLAS

Two years of GEOSAT altimeter observations are used to investigate the response of sea level to anomalous westerly wind bursts in the tropical Pacific Ocean before and during the 1986–87 El Niño. Sea level time series along the equator show examples of both positive and negative anomalies of 10-centimeter amplitude and 2- to 4-week time scale propagating across the Pacific with phase speeds of 2.4 to 2.8 meters per second, suggesting downwelling and upwelling Kelvin waves, respectively. A comparison of island wind observations with sea level indicates one instance (May 1986) in which a positive sea level anomaly can be related to westerly winds caused by a cross-equatorial cyclone pair in the western Pacific. This episode was followed by additional wind bursts later in the year, and finally by sustained westerlies in the western Pacific during November–December 1986, at the height of El Niño. The GEOSAT observations reveal the sea level response to these meteorological events and provide a synoptic description of the El Niño oceanographic phenomenon.

IT HAS BEEN SUGGESTED THAT THE onset of sea surface warming in the eastern tropical Pacific during an El Niño/Southern Oscillation (ENSO) event may be triggered by short, intense bursts of westerly winds in the western Pacific (*1, 2*). According to this scenario, anomalous westerlies generate downwelling Kelvin waves in the ocean, which then propagate eastward along the equator. Since these waves produce eastward zonal current anomalies and since the mean zonal sea surface temperature gradient is negative (colder eastward), surface temperatures in the eastern Pacific increase as a result of the advection of warm water zonally along the equator (*3, 4*).

Although other mechanisms may influence the development of an ENSO event, there are several reasons for believing that westerly wind bursts play a crucial role in the initial stages. Westerly bursts are known to occur more frequently in the western Pacific just before an ENSO event (*1*), often in association with the formation of cross-equatorial cyclone pairs (*2*). The sea level response to these bursts appears in tide gage records from island stations, primarily in the far western Pacific (*5*). Also, moored current meter records show that the passage of a Kelvin wave front generates eastward zonal transport in the surface mixed layer (*6*). Because of the vast size of the Pacific and the almost complete absence of islands in the eastern half, it has been difficult to document the oceanic response to these wind anomalies.

We examine 2 years of sea level time series along the equator in the Pacific based on observations obtained from the U.S. Navy altimeter satellite GEOSAT (*7, 8*). We first focus on one unusually strong westerly wind burst (May 1986), which forced a disturbance in sea level that propagated across the Pacific. This wind–sea level event is noteworthy because it led to several predictions of El Niño (*9–11*). We then examine how sea level behaved along the equator during the El Niño, which occurred later that year.

GEOSAT (GEOdetic SATellite), launched in March 1985, circles the earth 14 times per day and yields coverage between +72° and −72° latitude. Its radar altimeter provides a continuous record of sea level along the satellite ground track with a precision of approximately 3 cm. Previous work based on the limited sets of altimeter data collected in the 1970s (*12*) demonstrated

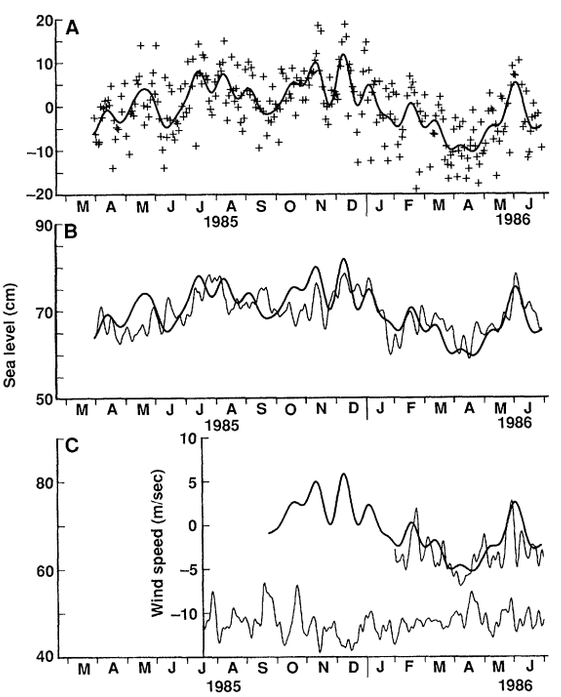

Fig. 1. (**A**) Sea level time series derived from 15 months of GEOSAT altimeter data near Christmas Island (2°N, 158°W). Crosses represent individual altimeter observations as determined by least-squares adjustment of crossover differences. The smooth curve shows an objective analysis fit to the same measurements, based on a decorrelation time scale of 15 days and a noise level of 5 cm. (**B**) Comparison of altimeter-derived sea level from (A) with low-pass filtered tide gage time series for Christmas Island. (**C**) Comparison of altimeter-derived sea level from (A) (heavy curve) with low-pass filtered east-west wind component for Nauru Island (upper light curve) and Christmas Island (lower light curve). The Nauru wind data have been offset in time by 23 days; the Christmas wind data have been offset in speed by 5 m/sec.

National Ocean Service, National Oceanic and Atmospheric Administration, Rockville, MD 20852.